SCIENCE CHINA
Information Sciences

• **RESEARCH PAPER** •

June 2023, Vol. 66 160404:1–160404:10
https://doi.org/10.1007/s11432-022-3695-1

Special Topic: Two-Dimensional Materials and Device Applications

Near-infrared optoelectronic synapses based on a Te/α-In_2Se_3 heterojunction for neuromorphic computing

Tao YAN[1,2†], Yuchen CAI[1,3†], Yanrong WANG[1,3], Jia YANG[1,3], Shuhui LI[1,3], Xueying ZHAN[1,3], Fengmei WANG[1,3], Ruiqing CHENG[4], Feng WANG[1,3*], Jun HE[4] & Zhenxing WANG[1,3*]

[1]*CAS Key Laboratory of Nanosystem and Hierarchical Fabrication, National Center for Nanoscience and Technology, Beijing* 100190, *China;*
[2]*Key Laboratory of Carbon Fiber and Functional Polymers, Ministry of Education, Beijing University of Chemical Technology, Beijing* 100029, *China;*
[3]*Center of Materials Science and Optoelectronics Engineering, University of Chinese Academy of Sciences, Beijing* 100049, *China;*
[4]*Key Laboratory of Artificial Micro- and Nano-Structures of Ministry of Education, School of Physics and Technology, Wuhan University, Wuhan* 430072, *China*

Received 10 October 2022/Revised 8 December 2022/Accepted 31 January 2023/Published online 10 May 2023

Abstract Neuromorphic computing based on artificial optoelectronic synapses has attracted considerable attention owing to its high time/power efficiency and parallel processing capability. However, existing devices are mainly suitable for only the visible range. Here, high-performance near-infrared optoelectronic memories and synapses were demonstrated using Te/α-In_2Se_3 heterostructures. Owing to the entangled ferroelectricity-semiconducting properties of α-In_2Se_3, whose ferroelectric polarizations can be switched by photocarriers that migrated from the Te near-infrared light absorber, the device could be set into a non-volatile high-resistance/low-resistance state through the application of positive gate voltages/near-infrared light pulses. Hence, the device could function as a high-performance photodetector, with a photoresponsive on/off ratio of $5.25 \times 10^4/8.3 \times 10^3$ and a specific detectivity of $2.6 \times 10^{11}/7.5 \times 10^{10}$ Jones at 1550/1940 nm. In addition, the device could function as a multi-state optoelectronic synapse with good stability and high linearity; moreover, using the device, we developed an optoelectronic artificial neural network with high recognition accuracies of 100% and 89.9% for a database composed of 64-pixel letters with 10% and 70% noise levels, respectively. Our work provides a feasible avenue for developing neuromorphic networks applicable in the infrared range.

Keywords near infrared, phototransistor, two-dimensional ferroelectric semiconductor, artificial neural networks, optoelectronic synapses

Citation Yan T, Cai Y C, Wang Y R, et al. Near-infrared optoelectronic synapses based on a Te/α-In_2Se_3 heterojunction for neuromorphic computing. Sci China Inf Sci, 2023, 66(6): 160404, https://doi.org/10.1007/s11432-022-3695-1

1 Introduction

In a traditional von Neumann computing architecture, the separation of the processing unit and the memory unit imposes an inherent upper limit on the computing speed and energy efficiency because the data shuttling process between the two units is time-consuming and energy-intensive. Therefore, this architecture becomes a bottleneck for thriving technologies that require the edge-processing of large amounts of data, including artificial intelligence, automobile driving, and the Internet of Things. In recent years, analog neuromorphic computing frameworks such as artificial neural networks (ANNs) have attracted much attention as promising candidates to break this well-known memory-wall limit owing

* Corresponding author (email: wangf@nanoctr.cn, wangzx@nanoctr.cn)
† Yan T and Cai Y C have the same contribution to this work.

© Science China Press 2023

to their computing-in-memory architecture with superior parallel processing performance [1–4]. ANNs based on various non-volatile memory devices, including two-terminal memristors [5–7], phase-change memories [8], and ferroelectric random-access memories [9], have been widely studied, and they have demonstrated great advantages, including strong fault tolerance, ultra-high computing speed, and ultra-low power consumption [10]. In particular, artificial optoelectronic synapses that mimic sensory neurons of the human retina have been proposed recently; they have shown promising possibilities in the perception, memorization, learning, and classification of incident light information [11–14]. The functions of the synapses are based on the electrical/optical programmable non-volatile conductance states, similar to the long-term plasticity of biological vision synapses [15]. In addition, optoelectronic synapses can sense and store optical information, enabling non-destructive weight modulation through remote light programming on single or multiple devices. However, existing optoelectronic synapses are mainly suitable for visible lights owing to the challenge of integrating bio-mimicking functions with narrow-bandgap materials.

Narrow-bandgap two-dimensional (2D) materials have shown great potential for the manufacture of next-generation infrared (IR) optoelectronic devices owing to their extraordinary properties and strong capability of van der Waals integration [16–22]. For example, tellurium (Te), a 2D semiconductor with a bandgap of 0.35 eV, shows various intriguing features, such as strong anisotropic absorption of IR lights [23], high charge carrier mobilities [24, 25], and topological Weyl nodes [26, 27]. Moreover, Te is stable in the atmosphere, which is an important advantage compared with other fragile narrow-bandgap 2D materials such as black phosphorus. However, the IR optoelectronic synapse based on Te has not been demonstrated.

Owing to the non-volatile and switchable polarization states under external electrical/optical stimuli, ferroelectric materials have attracted considerable attention as ultrafast and power-efficient non-volatile memories [9, 28, 29]. However, most of the traditional ferroelectric materials with wide bandgaps and low conductivities exhibit poor optoelectronic performance, so they are not suitable for constructing optoelectronic synapses. Fortunately, 2D ferroelectric semiconductors with bandgaps of < 2 eV and various new electronic and optoelectronic properties have been recently discovered [30–38]. Moreover, devices based on ferroelectric semiconductors show non-volatilely programmable conductance states owing to the entangled ferroelectricity and semiconducting properties [39–42]. For example, photodetectors based on ferroelectric semiconductor α-In_2Se_3 have shown ultra-high sensitivity and non-volatility under visible light stimulus [43]. Furthermore, an optoelectronic synapse based on α-In_2Se_3 with controllable temporal dynamics for multimode and multiscale reservoir computing has been recently demonstrated [44]. This means that optoelectronic synapses exhibit excellent properties in neuromorphic computing. However, α-In_2Se_3 has a bandgap of 1.4 eV, which limits its applications in the IR spectrum. To realize IR optoelectronic synapses, a promising strategy is to integrate 2D ferroelectric semiconductors, such as α-In_2Se_3, with a 2D IR-active layer, such as Te, so that the photogenerated charge carriers under IR light illumination can be injected from the IR-active layer to the ferroelectric layer.

Herein, high-performance near-infrared (NIR) optoelectronic memories and synapses were demonstrated using Te/α-In_2Se_3 heterostructures, where Te works as an NIR light absorber and α-In_2Se_3 as the channel of a ferroelectric semiconductor transistor. The heterostructure device was set into a non-volatile high-resistance state (HRS) through the application of positive gate voltages and non-volatile low-resistance states (LRSs) under NIR light illumination. Hence, the device could function as a high-performance NIR photodetector, with a photoresponsive on/off ratio of $5.25 \times 10^4/8.3 \times 10^3$, responsivity of 155.8/44.7 mA/W, and specific detectivity of $2.6 \times 10^{11}/7.5 \times 10^{10}$ Jones, at 1550/1940 nm, respectively. In addition, the device could function as a multi-state optoelectronic memory with good stability and endurance, and an optoelectronic synapse based on the device exhibited high linearity and repeatability. Using the device, we constructed an optoelectronic ANN with high recognition accuracies of 100% and 89.9% for a database composed of 64-pixel letters with 10% and 70% noise levels, respectively. Our work provides a feasible avenue for developing neuromorphic networks in the IR range.

2 Experimental section

Ultrathin and high-quality Te nanosheets were synthesized via chemical vapor deposition (Figure S1(a)) [45]. Te powder (purity of 99.99%) was used as the precursor. It was placed in the center of a horizontal quartz tube furnace, and the growth temperature was 370°C–400°C. The growth substrate was mica, which was placed at the downstream region of the horizontal quartz tube. To elimi-

nate the influence of oxygen, we purged the tube with 1000 sccm Ar for 10 min before heating. Afterward, Ar with a flow rate of 100 sccm and H_2 with a flow rate of 100 sccm were used as the carrier gas during the growth process. The furnace was then heated to 370°C–400°C and held for 30 min, and finally cooled to room temperature to obtain high-quality Te nanosheets on the mica substrate.

Heavily p-doped Si wafers covered with 90 nm SiO_2 were used as the substrates. They were cleaned using a piranha solution for 2 h at 120°C. An α-In_2Se_3 flake was exfoliated from its bulk crystal (99.995%, purchased from Shanghai Onway Technology Co., Ltd.), and then a Te flake grown on mica was wet-transferred onto the α-In_2Se_3. A poly (methyl methacrylate) (PMMA, 495 K, A5, Microchem Company) thin film was spin-coated on the mica substrate and baked at 100°C for 5 min. The PMMA film was peeled off from the mica substrate in deionized water, and the Te-containing PMMA film was transferred onto α-In_2Se_3. 8 nm Cr/80 nm Au electrodes were fabricated on the α-In_2Se_3 flake via electron-beam lithography and a thermal evaporation method. Finally, a 20 nm-thick Al_2O_3 capping layer was deposited on the device via atomic layer deposition at 150°C using trimethylaluminum and water as precursors. The top Al_2O_3 worked as an encapsulation layer to prevent the contamination of the 2D channels and enhance n-type doping (Figure S2).

The Te nanosheets were characterized via optical microscopy (OM, Olympus BX51M) and high-resolution transmission electron microscopy (HRTEM, Tecnai F20). The material's quality was measured via Raman microscopy (Renishaw InVia, 514 nm excitation laser). The flake thickness was measured via atomic force microscopy (AFM, Multimode 3D, Veeco, USA). The electrical and optoelectronic properties were characterized using a probe station coupled with a Keysight 1500A semiconductor analyzer system. All of the measurements were conducted under a high vacuum ($\sim10^{-6}$ Torr) to prevent the influence of the atmosphere.

3 Results and discussion

The schematic of the Te/α-In_2Se_3 heterostructure is shown in Figure 1(a). Te has a quasi-2D crystalline structure that is van der Waals stacked by one-dimensional chiral chains in the $\langle 0001 \rangle$ direction (Figures S1(b) and (c)). Figure S1(d) shows the OM image of the as-grown Te nanosheets. The nanosheets were mostly stripe-shaped, owing to the highly oriented growth process with the $\langle 0001 \rangle$ direction parallel with the mica substrate surface. A selected flake of Te was wet-transferred onto α-In_2Se_3 as an IR absorption layer. An Al_2O_3 layer was deposited as a capping layer.

The band profiles of Te and α-In_2Se_3 (Figure 1(b)) indicate that a type III band alignment was formed after the contact of Te and α-In_2Se_3 so that Te, with a narrow bandgap of 0.35 eV, can absorb lights of longer wavelengths. Moreover, photocarriers can migrate to α-In_2Se_3, affecting the ferroelectric polarization of α-In_2Se_3. The ferroelectricity of the exfoliated α-In_2Se_3 was confirmed via piezoresponse force microscopy at room temperature. The amplitude image (Figure 1(c)) shows two separated ferroelectric domains. Figure S3(b) shows the corresponding phase image, which shows a contrast of 180°, indicating that the adjacent domains exhibited opposite polarization directions. Both the amplitude and phase images are different from the topography image shown in Figure S3(a), eliminating the possible influence of height difference. In addition, the voltage sweeping curves featured apparent butterfly-shaped hysteresis loops, further confirming the ferroelectricity of α-In_2Se_3 (Figure 1(d)). Figures 1(e) and (f) show the output (the relationship between source-drain current and source-drain voltage, I_{DS}-V_{DS}) and transfer curves (the relationship between source-drain current and gate voltage, I_{DS}-V_{GS}) of a pure α-In_2Se_3 field-effect transistor (FET) in the dark state, respectively. The transfer curves indicate that the α-In_2Se_3 possessed an n-type semiconducting nature, with an on/off ratio of 10^5.

The elemental composition and uniformity of Te were confirmed via energy-dispersive X-ray spectroscopy (Figure 1(g)). Figure 1(h) shows the corresponding HRTEM image. The clear lattice fringe demonstrated uniform atomic arrangement with no significant point defects or dislocations, and the calculated lattice spaces of 0.22 and 0.60 nm corresponded to the $(1\bar{2}10)$ and (0001) planes, respectively. The inset is the corresponding selected-area electron diffraction pattern, which agrees well with the HRTEM results. The above results confirm the successful synthesis of high-quality Te single-crystal nanosheets. The typical output and transfer characteristic curves of the pure Te FET (Figures 1(i) and (j)) indicate that the as-grown Te was a p-type semiconductor.

We investigated the electronic and optoelectronic properties of Te/α-In_2Se_3 heterostructures. Figure 2(a) shows the AFM image and the corresponding line-scan profiles of a typical heterostructure

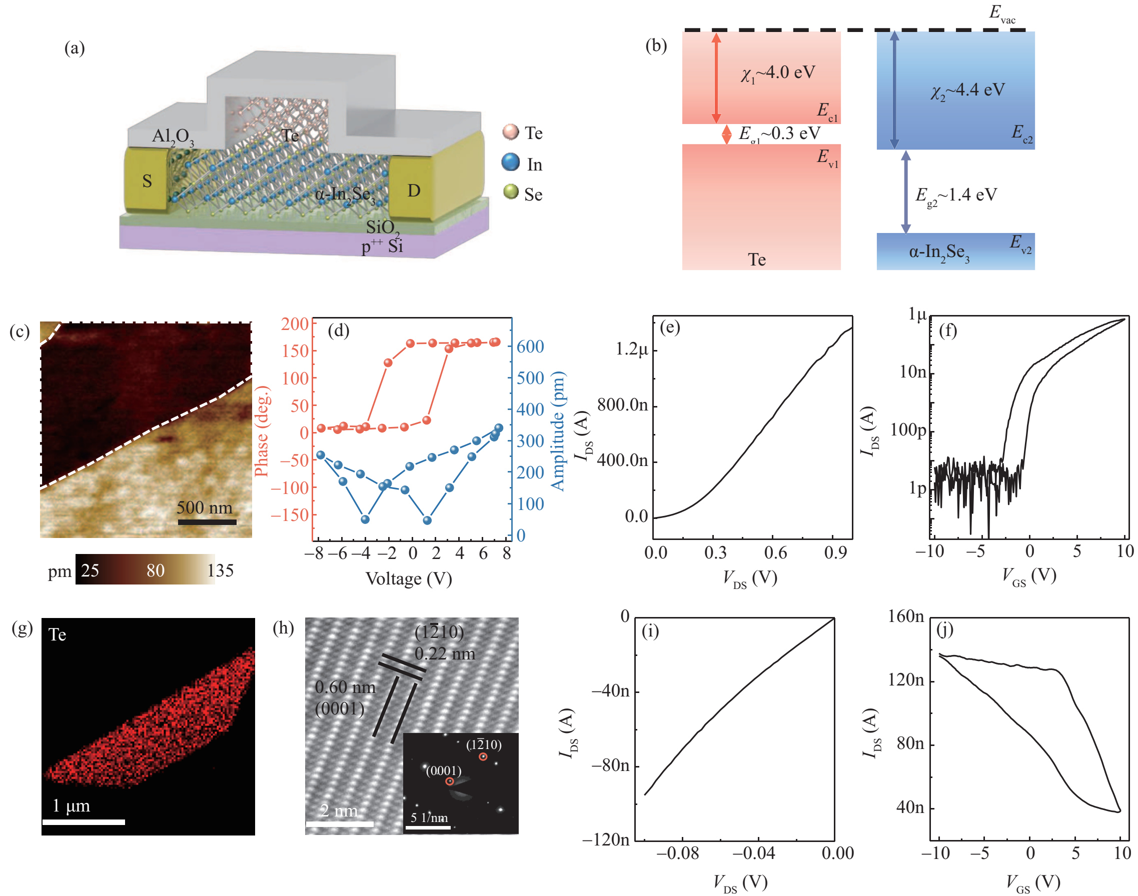

Figure 1 (Color online) (a) Schematic of the Te/α-In_2Se_3 van der Waals heterojunction. Source (S) and drain (D) electrodes were only in contact with α-In_2Se_3. Te was used as an NIR light absorber. Pink, blue, and yellow balls represent Te, In, and Se, respectively. (b) Band structures of Te and α-In_2Se_3 before contact. The work functions (χ) and bandgaps (E_g) are given. E_{vac}: the position of the vacuum level. (c) Piezoresponse force microscope (PFM) amplitude image of an α-In_2Se_3 flake on a heavily doped silicon substrate. The ferroelectric domain is marked by white dashed lines. (d) PFM amplitude and phase "butterfly" curves of the α-In_2Se_3 flake. I_{DS}-V_{DS} (e) and I_{DS}-V_{GS} (bias = 1 V) (f) characteristic curves of an α-In_2Se_3 field-effect transistor (FET) with 7 nm Al_2O_3 encapsulation (a 90 nm SiO_2 as the dielectric layer). (g) Energy-dispersive X-ray spectroscopy mapping of a Te nanoflake. (h) HRTEM image of the Te nanosheet. The inset shows the selected area electron diffraction pattern. I_{DS}-V_{DS} (i) and I_{DS}-V_{GS} (bias = 0.1 V) (j) characteristic curves of a Te FET with 90 nm SiO_2 as the dielectric. T = 80 K.

consisting of a 44 nm α-In_2Se_3 and a 32 nm Te. Figure S3(c) shows the Raman spectra of the heterostructure. The Raman spectrum of the junction region featured characteristic peaks corresponding to individual materials, indicating that the fabricated device possessed a good crystalline structure. Three electrodes were fabricated: terminals 1 and 2 on α-In_2Se_3 (source and drain terminal) and terminal 3 on Te. We could collect the properties of both the α-In_2Se_3 channel covered with a Te light absorber (between terminals 1 and 2) and the heterojunction (between terminals 1 and 3 or between terminals 2 and 3). Figures 2(b) and (c) show the transfer and output curves of α-In_2Se_3 (between terminals 1 and 2) under a gate voltage pulse of 10 V/−10 V and a 1550 nm light pulse. The transfer curves under the three states featured three threshold voltages with significant non-volatile shifts. In addition, to exclude the effect of the scanning process on the device, we varied the scanning range of the transfer curves and found that the scanning process had little effect on the current at zero gate voltage or threshold voltage (Figure S4). Accordingly, the device showed two non-volatile resistance states, an HRS and an LRS, at zero gate voltage (Figure 2(c)).

The properties of the heterojunction were also tested using terminals 2 and 3. Figure S3(d) shows the output curve, where V_{DS} was applied on terminal 3 (Te side) while terminal 2 (α-In_2Se_3) was kept grounded. The heterojunction exhibited significant rectification behavior with a higher current at the positive bias side. In addition, the heterojunction exhibited an anti-ambipolar property, as indicated by the transfer curve (Figure S3(e)), owing to gate-tunable charge carrier recombination at the van der Waals interface of the heterostructure [46, 47]. The above results demonstrate that a van der Waals

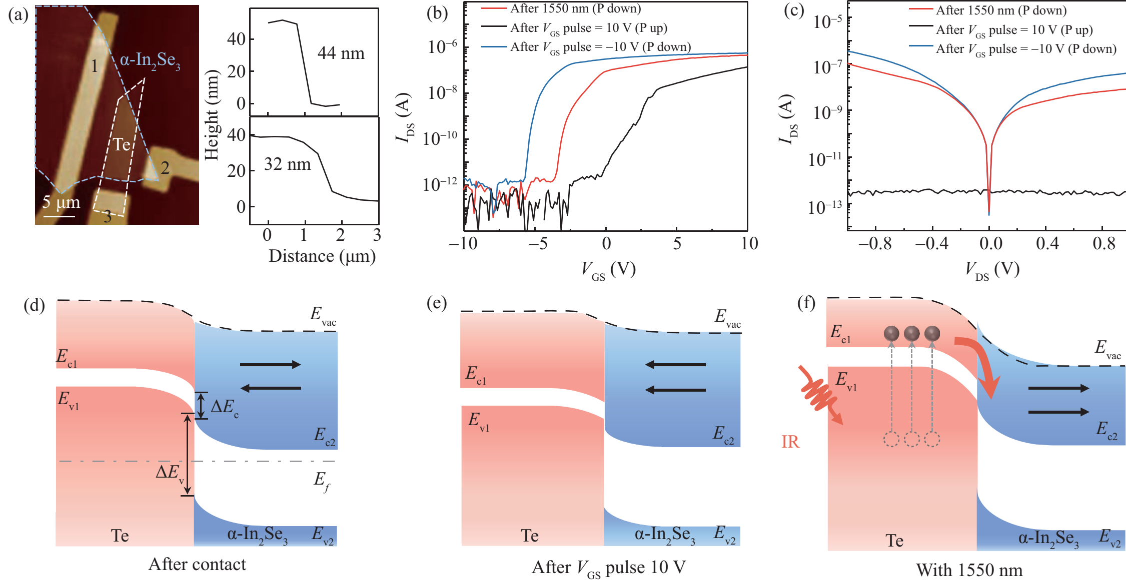

Figure 2 (Color online) (a) Left: AFM image of the α-In_2Se_3/Te heterostructure. The Te and α-In_2Se_3 flakes are marked with white and blue dashed lines, respectively. Right: Line scans of α-In_2Se_3 and Te. (b) Transfer and (c) output characteristics of the heterostructure after IR light and electrical stimulations. The pulse duration was 10 s, and the source-drain voltage was 1 V in (b). Energy band diagrams of the Te/α-In_2Se_3 after contact (d), after programming with a 10 V gate voltage pulse (e), and under 1550 nm light illumination (f). The black arrows indicate the ferroelectric polarization directions of α-In_2Se_3, and the red arrow represents the injection of photogenerated electrons from Te to α-In_2Se_3. The solid and open balls refer to electrons and holes, respectively. The conduction band edge (E_c), valence band edge (E_v), and energy steps (ΔE_c and ΔE_v) are indicated.

p–n junction was formed between the two 2D materials, and a built-in electric field directed from the α-In_2Se_3 to Te existed. Hence, the photocarriers generated at the Te side can be effectively injected into the α-In_2Se_3 channel under the effect of the built-in potential and NIR illumination.

The non-volatilely programmable resistance states can be explained by the electrically/optically switchable polarization states of α-In_2Se_3, which are schematically shown in Figures 2(d)–(f). After the contact of Te and α-In_2Se_3, band bending would occur at the heterostructure interface, considering that α-In_2Se_3 had a zero net polarization (Figure 2(d)). Under a positive gate voltage pulse, negative polarization charges were attracted to the dielectric layer to form an upward polarization state inside α-In_2Se_3 (Figure 2(e)). Therefore, the α-In_2Se_3 exhibited an HRS owing to electron depletion [31, 43]. In addition, the band bending degree was reduced because the direction of the downward depolarization field was opposite to that of the built-in electric field. In contrast, the application of a negative gate voltage will result in a downward polarization direction and an upward depolarization field to induce an LRS due to electron accumulation inside α-In_2Se_3.

Moreover, the ferroelectric polarization of α-In_2Se_3 can be reversed by light owing to the effect of photogenerated screening charges and/or an imprinting effect [37,41–43,48,49]. As depicted in Figure S5, the polarization-down state (corresponding to an LRS) featured lower energy compared with the polarization-up state (corresponding to an HRS). Hence, α-In_2Se_3 was usually transformed into a non-volatile LRS after light illumination [43]. However, owing to the wide bandgap of 1.4 eV, α-In_2Se_3 did not respond to IR light. Here, Te in Te/α-In_2Se_3 heterostructures can absorb IR light, and the generated electrons can migrate to α-In_2Se_3, crossing the interface, driven by the built-in electric field, resulting in a change in the α-In_2Se_3 polarization state (Figure 2(f)). The resistance state of the device can be non-volatilely programmed by both electrical and NIR light pulses. The time-dependent I_{DS} curve shown in Figure S3(f) depicts the non-volatile resistance switching behavior, where a $\sim 10^{-13}$ A HRS and a $\sim 10^{-9}$ A LRS with an on/off ratio of 4 orders of magnitude could be programmed under V_{GS} pulse = 4 V and 1550 nm light pulses with a density of 293 mW/cm^2. Four other devices exhibited a similar phenomenon (Figure S6).

Owing to the effect of the electrically/optically switchable resistance states, the Te/α-In_2Se_3 heterostructure can be used as a sensitive NIR photodetector. Figure 3(a) shows the I_{DS}-time characteristics with repeated positive gate and optical pulses (1550 nm at the top and 1940 nm at the bottom), whose waveforms are shown on the top side of the panel. The device exhibited a very low dark current of $\sim$1 pA at the HRS. Under irradiation by a 1550/1940 nm light for 5 s, the photocurrent increased and

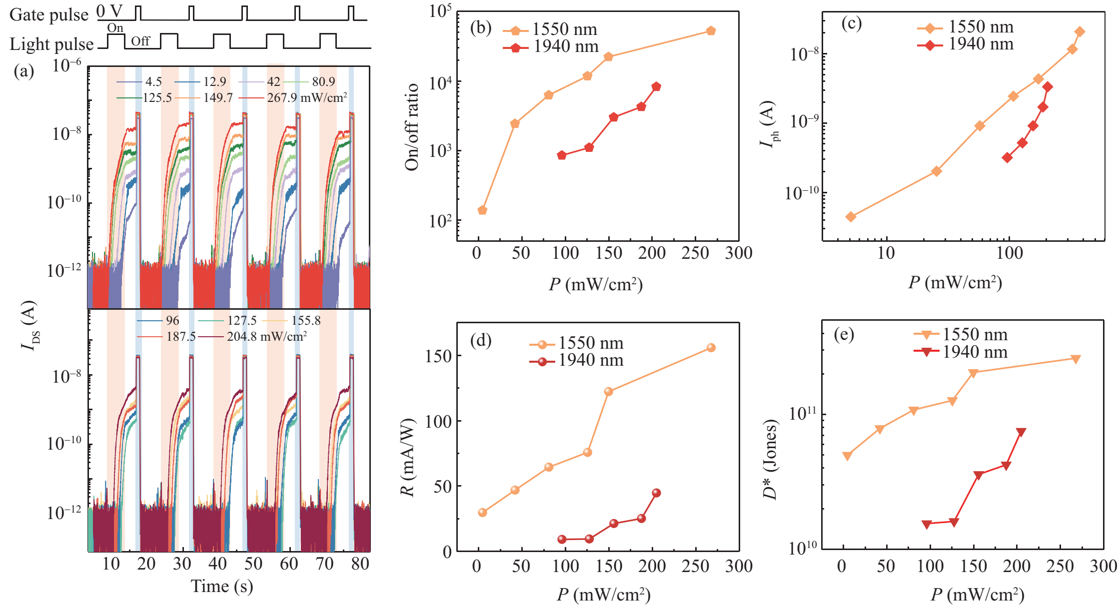

Figure 3 (Color online) (a) Time-dependent source-drain current ($I_{\rm DS}$) with five cycles of gate voltage (1 s) and IR light pulses (5 s). $V_{\rm DS}$ = 1 V. $V_{\rm GS}$ =1.2 V/1.8 V. Top: 1550 nm; Bottom: 1940 nm. (b)–(e) On-off ratio, photocurrent, responsivity (R), and detectivity (D^*) as a function of IR light power density. T = 80 K.

was almost maintained after the light was turned off. Subsequently, under a positive gate voltage pulse of 1.2/1.8 V, the device exhibited a stable HRS. For the resistance switching processes, the speed of the electrical pulse could be further increased to 50 ns (Figure S7), consistent with our previous work [40] in which pure α-In_2Se_3 phototransistors exhibited a similar speed. Owing to the very small dark current and high photocurrent, the device showed a high photoresponsive on/off ratio with a maximum value of 5.25×10^4 at 1550 nm and 8.3×10^3 at 1940 nm (Figure 3(b)). As shown in Figure 3(c), the photocurrent increased with increasing power density under light with different wavelengths, attributable to photocarrier-induced nucleation and growth of ferroelectric domains inside α-In_2Se_3. Most ferroelectric materials feature a multi-domain configuration, and the overall polarization depends on the dominant domain configuration. The higher the optical power densities, the higher the number of photocarriers produced by Te and the higher the number of electrons migrating into α-In_2Se_3. Hence, the switching of overall polarization could be induced through the reorientation of local domains, the nucleation of new domains, and/or the growth of existing domains in α-In_2Se_3 [50]. The device is different from a normal photodetector, in which the current will automatically return to its dark state. However, an ultrafast reset voltage pulse is acceptable for sensitive light detection just as a quench or reset circuit in a singlephoton avalanche diode [51].

The responsivity (R) was also calculated as $R = I_{\rm ph}/PS$, where $I_{\rm ph}$ is the photocurrent (defined as $I_{\rm illumination} - I_{\rm dark}$), P is the illumination power density, and S is the effective area (~35 μm²). R reached 155.8 and 44.7 mA/W for 1550 and 1940 nm light, respectively (Figure 3(d)). Under the assumption that the device noise was mainly from shot noise and that the dark current was the major contribution, specific detectivity (D^*) can be determined as $D^* = \frac{R\sqrt{S}}{\sqrt{2eI_{\rm dark}}}$. The maximum D^* values at 1550 and 1940 nm were 2.6×10^{11} and 7.5×10^{10} Jones, respectively (Figure 3(e)). Another device exhibited comparable performances, with a highest on/off ratio of 2.6×10^4, maximum responsivity of 56.9 mA/W, and maximum specific detectivity of 1.26×10^{12} Jones under 1550 nm IR light illumination (Figure S8). The above results indicate that the heterostructure had good IR detection performance. Low temperatures can stabilize the polarization/state and reduce the resistance and noise. This can be seen from time-dependent current curves obtained from a room temperature test (Figure S9), where the difference between the two resistance states quickly decreased from 3 orders to 1 order of magnitude, even with increasing pulse amplitude and width.

The application of both IR optical pulses and gate electrical pulses can cause a switch in the polarization states of the device and subsequently change its conductance states, which demonstrates the applicability of the device as a non-volatile optoelectronic memory. Figure 4(a) shows the time-dependent current after

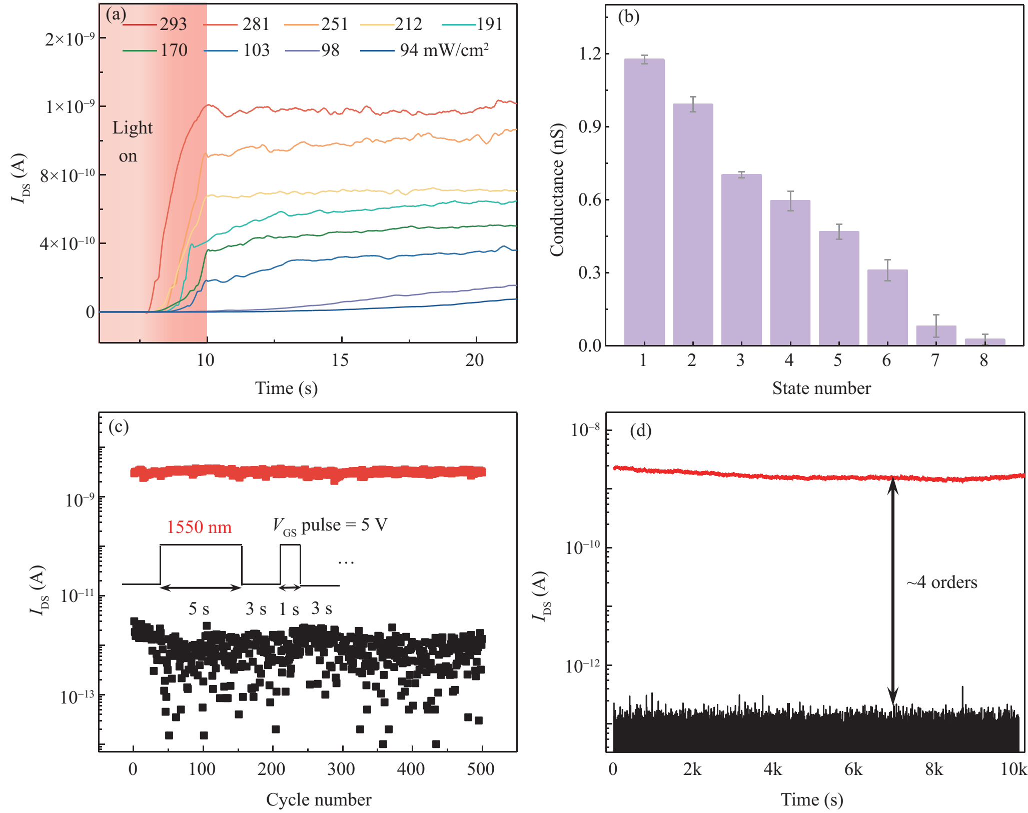

Figure 4 (Color online) (a) Time-dependent source-drain currents programmed under 1550 nm illumination with different power densities for 5 s. (b) Extracted eight conductance levels after IR pulse application. (c) Endurance characteristics of the device for over 500 cycles; the conditions included a 1550 nm light pulse with a 5 s duration, a power density of 293 mW/cm^2, and a 5 V gate voltage pulse with a 1 s duration. The intervals between the two pulses were 3 s. (d) Retention properties of the two resistance states. V_{DS} = 1 V, T = 80 K.

under 1550 nm light pulses with various densities. The greater the power density, the greater the resulting current, and the current states were maintained after light removal. The response of the device under weak light was also stable (Figure S10(a)), which indicates that our heterostructure devices showed good stability. In addition, Figure S10(b) shows the performance of another device, whose states were also stable. The extracted conductance distribution exhibited good linearity (Figure 4(b)). Another device exhibited similar results (Figure S10). Moreover, optical and electrical pulse-switching cycle tests were conducted. The device was set to an LRS through the application of a 1550 nm IR light pulse with a density of 293 mW/cm^2 and 5 s duration, and then an electrical pulse of 5 V was applied for 1 s to set the device to an HRS, and the intervals between the two pulses were 3 s. After 500 cycles of LRS-HRS switching, the device still maintained significant LRS and HRS with only a small conductance shift (Figure 4(c)). Finally, we analyzed the device conductance under optical and electrical pulses. The device exhibited stable LRS and HRS states; an on/off ratio of 4 orders of magnitude could be kept for over 10000 s, demonstrating the good retention ability of the device (Figure 4(d)). The difference between the LRSs depicted in Figures 4(c) and (d) originated from the different durations of electrical pulses. The stable conductance, high on/off ratio, and multi-state performance indicate that an optoelectronic synapse working in the NIR spectrum can be realized using this device.

Finally, we demonstrate the performance of an optoelectronic ANN based on our device. The ANN consisted of three layers: 64 input neurons corresponding to an input NIR image with 8 × 8 pixels, 36 hidden neurons, and 4 output neurons corresponding to the recognition scores of four letters (Figure 5(a)). Connections between neighboring neuron layers (i.e., artificial synapses) were weighted according to the conductance states of the device. The output scores were activated summation values of the hidden neurons with a soft-max activation function, and the highest score among the four outputs indicated the letter to which the input image belonged. Owing to the programmability of the Te/α-In_2Se_3 optoelectronic memory, the long-term potentiation (LTP) and long-term depression (LTD) behavior can be achieved using optical and positive electrical pulses, respectively. To realize a linear update of weights and avoid

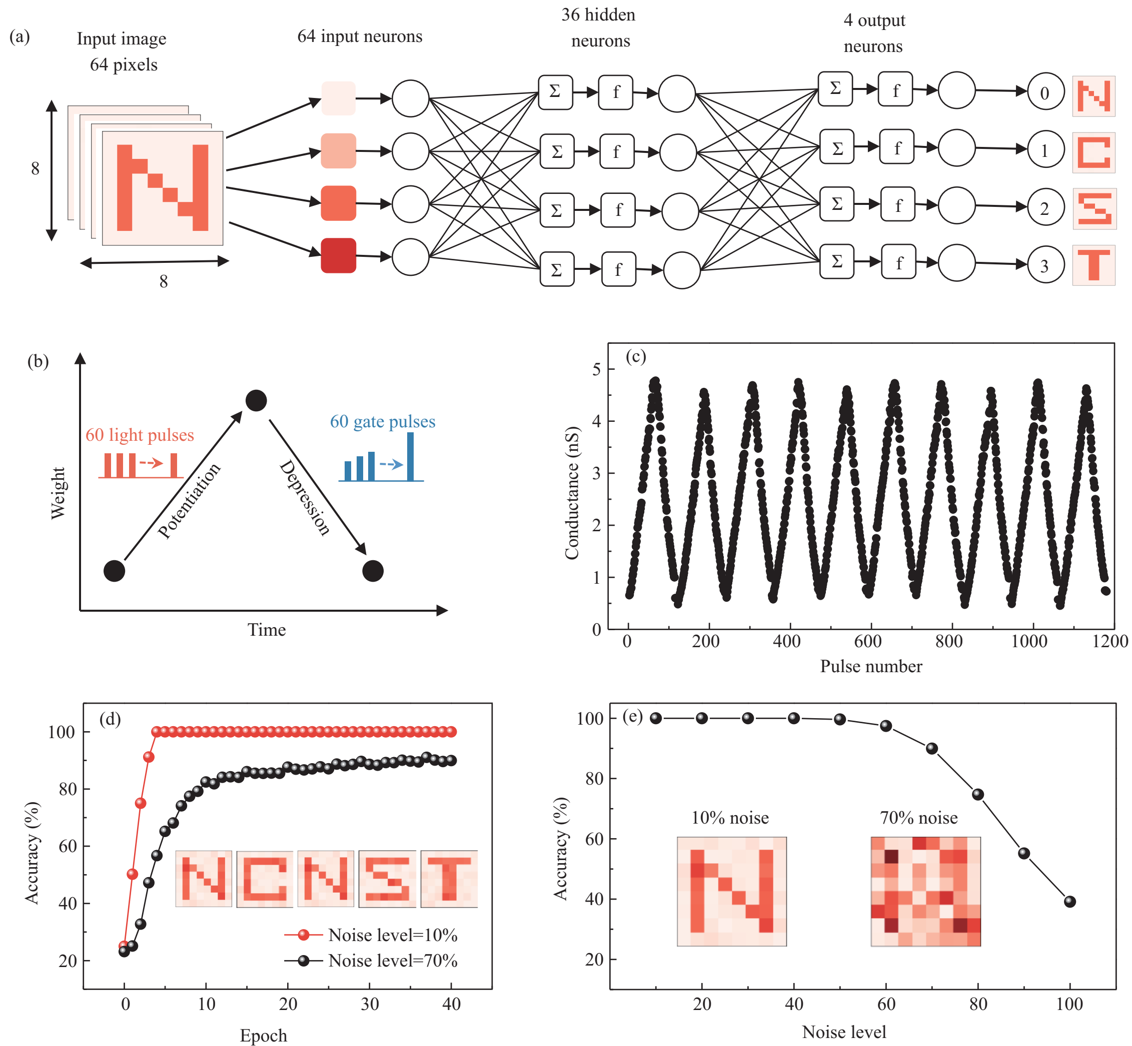

Figure 5 (Color online) (a) Schematic of a three-layer ANN for recognizing different letters with 8 × 8 pixels. (b) Weights updated as a function of the number of potentiation and depression pulses. (c) Long-term potentiation/long-term depression signatures of the device after the application of continuous IR light and electrical pulses. The light pulse was 293 mW/cm^2 with a width of 25 ms, and the electrical pulse was 0.9 V–1.8 V with a step of 0.015 V. (d) Training results on pictures of letters with 10% and 70% Gaussian noise levels. The images shown in the inset are various letters with 10% noise. (e) Relationship between recognition accuracy and noise level. The inset shows an image with 10% noise and 70% noise.

unwanted mutation of the potentiation and depression processes, the training process was conducted using optical/electrical pulses with short intervals (Figure 5(b)). LTP was tested through under 1550 nm IR pulses with a width of 25 ms and amplitude of 293 mW/cm^2. LTD was tested under positive gate voltage pulses with a width of 10 ms and variable amplitudes of 0.9–1.8 V, with a step of 0.015 V. The device demonstrated good repeatability in terms of linearly modulated symmetric LTP and LTD states for 10 cycles (Figure 5(c)), which is essential to realize high-accuracy neuromorphic computing for image classification. The device was non-volatile to pulses. When a light pulse was applied, the photocurrent of the device increased, and when the light pulse was removed, the current remained in a certain state. Thus, over time, the current varied in a stepwise manner (Figure S11). We also programmed a similar device with all-electric pulses (Figure S12). Owing to the good linearity, low variation among cycles, and the occurrence of numerous states, the constructed ANN exhibited high accuracy.

The simulated on-chip training process of our neuromorphic computing model was based on the above-described experimental results, and the pulse number was defined by a backpropagation algorithm. At each training epoch, a dataset containing 10000 images was fed into the model, and the weights were updated according to a backpropagation loss function. The simulation results are shown in Figures 5(d) and (e). Even at a noise level of up to 70%, the recognition accuracy was 89.9% after 40 epochs of training, which demonstrates the strong noise tolerance of the device. Moreover, the device could accurately

recognize the letters "NCNST" at a 10% noise level (the inset of Figure 5(d)). Figure S13(c) shows the accuracy evolution depending on the training epoch at all selected noise levels. Because of the good linearity and repeatability of our devices, high recognition accuracy was maintained at a 90% noise level (see Figure 5(e) and S14). The self-built database contained 10000 and 2000 images for training and testing, respectively, and the constructed ANN was fault-tolerant over image recognition tasks, which resulted in high accuracy. Moreover, to provide standard performance evaluation, the constructed neuromorphic model could also be used to recognize more complicated images from the Fashion-MNIST (F-MNIST) dataset (Figure S15); a recognition accuracy of 82.7% was reached after 40 epochs. Similar results were achieved through the combination of 1940 nm IR pulses and electrical pulses (Figure S16).

4 Conclusion

High-performance NIR optoelectronic memories and artificial synapses were fabricated using Te/α-In_2Se_3 heterostructures, where Te functioned as an NIR light absorber and α-In_2Se_3 as the channel of a ferroelectric semiconductor transistor. We synthesized high-quality single-crystalline Te nanosheets via chemical vapor deposition and constructed heterostructures with exfoliated α-In_2Se_3. Owing to the entangled ferroelectricity and semiconducting properties of α-In_2Se_3, the device could be set into a non-volatile HRS with a stable current of 1 pA under positive gate voltages. In addition, because the built-in potential exits at the hetero-interface, photocarriers generated in the Te could migrate to α-In_2Se_3 under NIR light illuminations, and then the device could switch into an LRS. Hence, the device could achieve high-performance NIR detection, with a photoresponsive on/off ratio of $5.25 \times 10^4/8.3 \times 10^3$, responsivity of 155.8/44.7 mA/W, and specific detectivity of $2.6 \times 10^{11}/7.5 \times 10^{10}$ Jones at 1550/1940 nm, respectively. In addition, the device could function as a multi-state optoelectronic memory with good stability (10^4 s) and endurance (for over 100 cycles). Thus, an optoelectronic synapse based on the device exhibited high linearity and repeatability, and a prototypical neuromorphic network was developed. The optoelectronic ANN exhibited high recognition accuracies of 100% and 89.9% for a database of 64-pixel letters with 10% and 70% noise levels, respectively. Our work demonstrates the potential application of ferroelectric semiconductor heterostructures for the development of wide-band optoelectronic neural networks.

Acknowledgements This work was supported by National Key R&D Program of China (Grant Nos. 2021YFA1201500, 2018YFA-0703700), National Natural Science Foundation of China (Grant Nos. 91964203, 61974036, 62274046, 22179029, 12204122), Strategic Priority Research Program of Chinese Academy of Sciences (Grant Nos. XDB44000000), Fundamental Research Funds for the Central Universities (Grant No. 2042021kf0067), and CAS Key Laboratory of Nanosystem and Hierarchical Fabrication. The authors also gratefully acknowledge the support of Youth Innovation Promotion Association CAS.

Supporting information Figures S1–S16. The supporting information is available online at info.scichina.com and link.springer.com. The supporting materials are published as submitted, without typesetting or editing. The responsibility for scientific accuracy and content remains entirely with the authors.

References

1 Indiveri G, Liu S C. Memory and information processing in neuromorphic systems. Proc IEEE, 2015, 103: 1379–1397
2 Yao P, Wu H, Gao B. Face classification using electronic synapses. Nat Commun, 2017, 8: 15199
3 Ielmini D, Wong H S P. In-memory computing with resistive switching devices. Nat Electron, 2018, 1: 333–343
4 Zidan M A, Strachan J P, Lu W D. The future of electronics based on memristive systems. Nat Electron, 2018, 1: 22–29
5 Yao P, Wu H, Gao B. Fully hardware-implemented memristor convolutional neural network. Nature, 2020, 577: 641–646
6 Li C, Hu M, Li Y. Analogue signal and image processing with large memristor crossbars. Nat Electron, 2017, 1: 52–59
7 Xia Q, Yang J J. Memristive crossbar arrays for brain-inspired computing. Nat Mater, 2019, 18: 309–323
8 Tuma T, Pantazi A, Gallo M L. Stochastic phase-change neurons. Nat Nanotech, 2016, 11: 693–699
9 Khan A I, Keshavarzi A, Datta S. The future of ferroelectric field-effect transistor technology. Nat Electron, 2020, 3: 588–597
10 Wan W, Kubendran R, Schaefer C. A compute-in-memory chip based on resistive random-access memory. Nature, 2022, 608: 504–512
11 Kim M S, Kim M S, Lee G J. Bio-inspired artificial vision and neuromorphic image processing devices. Adv Mater Technologies, 2021, 7: 2100144
12 Zhou F, Zhou Z, Chen J. Optoelectronic resistive random access memory for neuromorphic vision sensors. Nat Nanotechnol, 2019, 14: 776–782
13 Jin C, Liu W, Xu Y. Artificial vision adaption mimicked by an optoelectrical In_2O_3 transistor array. Nano Lett, 2022, 22: 3372–3379
14 Hou Y X, Li Y, Zhang Z C. Large-scale and flexible optical synapses for neuromorphic computing and integrated visible information sensing memory processing. ACS Nano, 2021, 15: 1497–1508
15 Kolb H. How the retina works. Am Sci, 2003, 91: 28–35
16 Yan Z Z, Jiang Z H, Lu J P. Interfacial charge transfer in WS_2 monolayer/$CsPbBr_3$ microplate heterostructure. Front Phys, 2018, 13: 138115
17 Chen Y, Tan C, Wang Z, et al. Momentum-matching and band-alignment van der Waals heterostructures for high-efficiency infrared photodetection. Sci Adv, 2022, 8: eabq1781

18 Lee S, Peng R, Wu C. Programmable black phosphorus image sensor for broadband optoelectronic edge computing. Nat Commun, 2022, 13: 1485
19 Jiao H, Wang X, Chen Y, et al. HgCdTe/black phosphorus van der Waals heterojunction for high-performance polarization-sensitive midwave infrared photodetector. Sci Adv, 2022, 8: eabn1811
20 Li N, Wen Y, Cheng R. Strongly coupled van der Waals heterostructures for high-performance infrared phototransistor. Appl Phys Lett, 2019, 114: 103501
21 Xu G, Liu D, Li S. Binary-ternary transition metal chalcogenides interlayer coupling in van der Waals type-II heterostructure for visible-infrared photodetector with efficient suppression dark currents. Nano Res, 2021, 15: 2689–2696
22 Luo P, Liu C, Lin J. Molybdenum disulfide transistors with enlarged van der Waals gaps at their dielectric interface via oxygen accumulation. Nat Electron, 2022, 5: 849–858
23 Tong L, Huang X, Wang P. Stable mid-infrared polarization imaging based on quasi-2D tellurium at room temperature. Nat Commun, 2020, 11: 2308
24 Wang Y, Qiu G, Wang R. Field-effect transistors made from solution-grown two-dimensional tellurene. Nat Electron, 2018, 1: 228–236
25 Zhao C, Tan C, Lien D H. Evaporated tellurium thin films for p-type field-effect transistors and circuits. Nat Nanotechnol, 2020, 15: 53–58
26 Hirayama M, Okugawa R, Ishibashi S. Weyl node and spin texture in trigonal tellurium and selenium. Phys Rev Lett, 2015, 114: 206401
27 Qiu G, Niu C, Wang Y. Quantum hall effect of Weyl fermions in n-type semiconducting tellurene. Nat Nanotechnol, 2020, 15: 585–591
28 Martin L W, Rappe A M. Thin-film ferroelectric materials and their applications. Nat Rev Mater, 2016, 2: 16087
29 Chen C, Yang M, Liu S, et al. Bio-inspired neurons based on novel leaky-FeFET with ultra-low hardware cost and advanced functionality for all-ferroelectric neural network. In: Proceedings of Symposium on VLSI Technology, 2019
30 Xiao J, Zhu H, Wang Y. Intrinsic two-dimensional ferroelectricity with dipole locking. Phys Rev Lett, 2018, 120: 227601
31 Si M, Saha A K, Gao S. A ferroelectric semiconductor field-effect transistor. Nat Electron, 2019, 2: 580–586
32 Wang L, Wang X, Zhang Y. Exploring ferroelectric switching in α-In_2Se_3 for neuromorphic computing. Adv Funct Mater, 2020, 30: 2004609
33 Xue F, Hu W, Lee K C. Room-temperature ferroelectricity in hexagonally layered α-In_2Se_3 nanoflakes down to the monolayer limit. Adv Funct Mater, 2018, 28: 1803738
34 Ding W, Zhu J, Wang Z. Prediction of intrinsic two-dimensional ferroelectrics in In_2Se_3 and other III_2-VI_3 van der Waals materials. Nat Commun, 2017, 8: 14956
35 Hu H, Sun Y, Chai M. Room-temperature out-of-plane and in-plane ferroelectricity of two-dimensional β-InSe nanoflakes. Appl Phys Lett, 2019, 114: 252903
36 Chang K, Liu J, Lin H. Discovery of robust in-plane ferroelectricity in atomic-thick SnTe. Science, 2016, 353: 274–278
37 Li T, Lipatov A, Lu H. Optical control of polarization in ferroelectric heterostructures. Nat Commun, 2018, 9: 3344
38 Wu S, Chen Y, Wang X. Ultra-sensitive polarization-resolved black phosphorus homojunction photodetector defined by ferroelectric domains. Nat Commun, 2022, 13: 3198
39 Xu K, Jiang W, Gao X. Optical control of ferroelectric switching and multifunctional devices based on van der Waals ferroelectric semiconductors. Nanoscale, 2020, 12: 23488–23496
40 Xue F, He X, Liu W. Optoelectronic ferroelectric domain-wall memories made from a single van Der Waals ferroelectric. Adv Funct Mater, 2020, 30: 2004206
41 Hu W J, Wang Z, Yu W. Optically controlled electroresistance and electrically controlled photovoltage in ferroelectric tunnel junctions. Nat Commun, 2016, 7: 10808
42 Long X, Tan H, Sánchez F. Non-volatile optical switch of resistance in photoferroelectric tunnel junctions. Nat Commun, 2021, 12: 382
43 Yang J, Wang F, Guo J. Ultrasensitive ferroelectric semiconductor phototransistors for photon-level detection. Adv Funct Mater, 2022, 32: 2205468
44 Liu K, Zhang T, Dang B. An optoelectronic synapse based on α-In_2Se_3 with controllable temporal dynamics for multimode and multiscale reservoir computing. Nat Electron, 2022, 5: 761–773
45 Yao Y, Zhan X, Ding C. One-step method to simultaneously synthesize separable Te and GeTe nanosheets. Nano Res, 2022, 15: 6736–6742
46 Lee C H, Lee G H, van der Zande A M. Atomically thin p-n junctions with van der Waals heterointerfaces. Nat Nanotech, 2014, 9: 676–681
47 Wang F, Wang Z, Xu K. Tunable GaTe-MoS_2 van der Waals p-n junctions with novel optoelectronic performance. Nano Lett, 2015, 15: 7558–7566
48 Kreisel J, Alexe M, Thomas P A. A photoferroelectric material is more than the sum of its parts. Nat Mater, 2012, 11: 260
49 Wang J L, Vilquin B, Barrett N. Screening of ferroelectric domains on $BaTiO_3$ (001) surface by ultraviolet photo-induced charge and dissociative water adsorption. Appl Phys Lett, 2012, 101: 092902
50 Stolichnov I, Tagantsev A, Setter N. Crossover between nucleation-controlled kinetics and domain wall motion kinetics of polarization reversal in ferroelectric films. Appl Phys Lett, 2003, 83: 3362–3364
51 Takai I, Matsubara H, Soga M. Single-photon avalanche diode with enhanced NIR-sensitivity for automotive LIDAR systems. Sensors, 2016, 16: 459